geosciences

MDPI

Article

Study of Corrosion Resistance Properties of Heat Exchanger Metals in Two Different Geothermal Environments

Svava Davíðsdóttir [1], Baldur Geir Gunnarsson [1], Kjartan Björgvin Kristjánsson [1], Béatrice A. Ledésert [2] and Dagur Ingi Ólafsson [1,*]

[1] Tæknisetur ehf, Árleynir 2-8, 112 Reykjavík, Iceland; svava@taeknisetur.is (S.D.); baldur@taeknisetur.is (B.G.G.); kjartan@taeknisetur.is (K.B.K.)
[2] GEC Laboratory, CY Cergy Paris Université, 1 Rue Descartes, 95000 Neuville Sur Oise, France; beatrice.ledesert@cyu.fr
* Correspondence: dagur@taeknisetur.is

Abstract: Geothermal fluids harnessed for electricity production are generally corrosive because of their interaction with the underground. To ensure the longevity and sustainability of geothermal Organic Rankine Cycle (ORC) powerplants, the choice of heat exchanger material is essential. The performance of heat exchangers is affected by corrosion and scaling due to the geothermal fluids, causing regular cleaning, part replacement, and in the worst cases, extensive repair work. The properties of geothermal fluids vary between geothermal settings and even within geothermal sites. Differences in exposure conditions require different material selection considerations, where factors such as cost, and material efficiency are important to consider. This work studies in-situ geothermal exposure testing of four metals at two geothermal locations, in different geological settings. Four corrosion-resistant materials were exposed for one month at Reykjanes powerplant in Iceland and four months at Chaunoy oil field in France as material candidates for heat exchangers. The tested alloys were analysed for corrosion with macro- and microscopic techniques using optical and electron microscopes, which give an indication of the different frequencies of repairs and replacement. Inconel 625 showed no effects at Reykjanes and cracks at Chaunoy. The others (316L, 254SMO, and titanium grade 2) showed either corrosion or erosion traces at both sites.

Keywords: geothermal; oil; heat exchanger; corrosion; scaling; geology

Citation: Davíðsdóttir, S.; Gunnarsson, B.G.; Kristjánsson, K.B.; Ledésert, B.A.; Ólafsson, D.I. Study of Corrosion Resistance Properties of Heat Exchanger Metals in Two Different Geothermal Environments. *Geosciences* **2021**, *11*, 498. https://doi.org/10.3390/geosciences11120498

Academic Editors: Romain Augier, Thomas Hermans and Jesus Martinez-Frias

Received: 8 October 2021
Accepted: 2 December 2021
Published: 7 December 2021

1. Introduction

Material selection for geothermal equipment is a crucial parameter to consider when constructing an Organic Rankine Cycle (ORC) geothermal power plant. The heat exchanger transfers heat energy from the geothermal power source to the organic fluid within the closed loop of the ORC, boiling it. The organic fluid in its vapour form is then used to transfer the energy to the turbines of the ORC plant, generating electricity, before being condensed to repeat the continuous cycle. Geothermal environments differ between locations and the material selection for the heat exchanger needs to be tailored for each environment. The geothermal fluids can be challenging for heat exchanger materials due to high velocity, abrasive particles, reactive gasses such as H_2S, and in some cases salinity [1,2].

The focus of the current study is to investigate heat exchange plate candidates, metals, and metal alloys which are more prone to local corrosion rather than uniform corrosion. Local corrosion is often associated with metals and metal alloys forming natural passivation layers, which protect the surface of the metal. The performance of the metals and alloys is often dependent on its natural initial passivation layer and its ability to re-passivate if it gets attacked during operation. Alloying elements such as Cr and Mo form protective oxides at the metal surface [3]. Furthermore, the amount of Cr and Mo within the alloy is often used for ranking the alloys with pitting resistance equivalent number (PRE) [4].

Oxygen is rarely present within the geothermal fluid of heat exchange systems and if it is, special precautions need to be taken [5]. Gasses such as CO_2 and H_2S are common in geothermal environments [2,6].

The surface area and thermal conductivity of the heat exchanger plates are crucial for optimising the efficiency of the heat transfer. Scaling and corrosion often result in insulating layers forming on the surface of the plates, which reduce the heat transfer efficiency from the geothermal fluid. Scaling and corrosion are therefore important to avoid or minimize.

There are three main failure mechanisms of a heat exchanger: leakages, blocking due to deposits, and material thinning [7]. The main reasons for material thinning are erosion and corrosion. Erosion is caused by mechanical abrasion which results in mechanical removal of the surface material. Erosion depends on fluid velocity and the presence of abrasive particles in the fluid [7]. There is a correlation between material hardness and erosion resistance [8]. To minimize maintenance costs, production downtime, and part replacement in geothermal power plants, it is important to study the corrosion, erosion, and scaling issues affecting the various equipment in contact with the geothermal brine and to acquire a better understanding of how to ensure the sustainability of the plants. In the case of ORC power plants, the main equipment in contact with the geothermal brine are heat exchangers.

The majority of geothermal power plants, and especially those that run on the ORC principle, operate at low or medium temperatures, below 200 °C. This is reflected in the demonstration sites of the MEET H2020 project (Multidisciplinary and multi-context demonstration of Enhanced geothermal systems exploration and Exploitation Techniques and potentials) to which this study is dedicated, such as Soultz-sous-Forêts, Grásteinn, Cazaux, Chaunoy, and Krauma. Various corrosion and scaling studies have been conducted at Soultz-sous-Forêts where the geothermal fluid is quite saline, corrosive, and tends to form scales which accumulate naturally occurring radioactive materials [9–12]. Ledésert et al. [13] studied the scaling formation at Soultz-sous-Forêts when the reinjection temperature of the geothermal fluid was reduced from 70 °C to 40 °C. They concluded that the scaling formation observed was not influenced by the alloy of the heat exchanger material.

In recent years, several material experiments have been conducted at supercritical temperatures [14,15] where the conditions vary significantly from standard geothermal plants. For geothermal power plants operating at a low or medium temperature a few studies have been published [16–18] but no review paper is available. For a tailored material selection, a common evaluation method is to expose material candidates in the actual geothermal environment. It is recommended for material evaluation that the samples be tested for as long as possible although commonly it is based on the convenience of the plant operators [19]. Frequently, test durations range from a month and upwards. The exposure time is short compared to the lifetime of the material but gives an indication of the performance of the material in the actual environment. The most common method to evaluate exposed materials for geothermal applications is with weight loss measurements using standard ASTM G1-03, which estimates uniform corrosion. However, the materials evaluated in this study are more prone to local corrosion.

Metal and metal alloys forming natural passivation layers are more often affected by local corrosion than uniform corrosion. The passivation layer is locally broken, resulting in the direct electrical contact of the metal with the fluid. The fluid can either be in liquid or vapour form depending on the temperature and pressure. Geothermal fluids usually contain ions which increase their conductivity which can accelerate corrosion [2]. Furthermore, Cl ions in connection with oxygen and water have been reported to assist with the breakdown of the passivation layer of stainless steel resulting in corrosion [20]. For example, 316L stainless steel has been reported to have low performance in humid and oxygen rich environments; however, it has been successfully used in oxygen free CO_2 brines at temperatures as high as 150 °C [21].

The 316L and 304L are some of the most used and studied materials in the geothermal industry and are widely used in heat exchangers [5]. Nickel alloys have shown promising

results in the S rich environment and Ti and its alloys in an oxygen rich environment [5,22]. However, due to the lower hardness of pure Ti, its alloys are often preferred for the geothermal environment [23,24]. Furthermore, from the oil and gas industry it is reported that the main failure mechanism of Ni-based alloy is from hydrogen embrittlement [25]. It has been reported by Karlsdóttir et al. [14] that the most corrosive resistant material tested for geothermal heat exchange application in superheated geothermal steam was Inconel 625 and Ti-alloy (Ti gr. 7). Furthermore, the group reported that 254SMO had a corrosion rate of 0.001 mm/year measured according to ASTM G1-03 [14], which is in line with results from the same group's measuring in simulated superheated geothermal conditions' corrosion rate of 0.001 mm/year [26]. Therefore, 254SMO has been recommended to be used by the Icelandic geothermal industry [10]. However, due to its cost it is not as commonly used in geothermal environments [27] as other cheaper materials such as 316L, for example.

The pH of the fluid is an important factor for determining the lifetime of components and 316L is, for example, not recommended to be used at a pH lower than 3.2 [28] where superaustenitic steels, such as 254SMO, can be a good option [29]. For geothermal applications, stainless steels and Ni-alloys are recommended to have a minimum of 3% Mo [30]. However, high levels of Mo could result in more risk for inducing segregation, the formation of hard and brittle phases within the material, which could initiate cracks and voids during exposure [31]. The grain size of steel can be crucial as smaller grain size can reduce interdenritic segregation as well as the chances of high temperature cracking [32]. Inclusions are common within stainless steels and have been reported to be found in 254SMO [31,32] and 316 [33]. The inclusions can be a preferential place for crack development at the subsurface of the material [33]. Inclusions can create geometric discontinuities where stress and strain can accumulate [34]. Moreover, for surfaces with a passive layer, an inclusion might act as an initiation site for pitting [35].

To identify suitable materials for heat exchangers in low-temperature volcanic and sedimentary ORC power plants, four metal samples were exposed in two different geothermal environments, namely at high salinity locations in Reykjanes, Iceland and Chaunoy, France. The effects on the coupons were then examined macro- and microscopically. The selected materials consisted of stainless steels 316L (EN 1.4404) and 254SMO (EN 1.4547), nickel alloy Inconel 625 (EN 2.4856), and titanium grade 2 (EN 3.7035). All these materials are reported to be used in the geothermal industry [29]. In general, failure during the plate heat exchange operation accrues in the weakest points of the material. Additionally, the materials studied here are more prone to local corrosion than uniform corrosion. Therefore, the main interest of this study is to investigate the most affected areas of the exposed materials and report on the observed local corrosion. The testing period was one and four months, respectively, for Reykjanes and Chaunoy, while the expected lifetime of a heat exchanger is around 20–30 years. All samples tested were affected by the exposure, including 254SMO and Inconel 625. Further investigation is needed to determine the development of the defects found after the exposure.

1.1. Geological Context

1.1.1. Reykjanes

Iceland began to form in Tertiary (16 Ma) [36] and is considered to be the product of anomalously high volcanism related to the interaction of the divergent plate boundaries on the Mid-Atlantic Ridge (MAR) and the Iceland mantle plume [37]. The MAR cuts across Iceland in a roughly SW-NE trending direction and at the crest of it is where the most vigorous magmatic activity occurs. Thus, numerous active volcanic systems can be found along the ridge axis [38]. The Reykjanes Peninsula, in SW Iceland, is a continuation of the median fault zone of the MAR and continues as Reykjanes Ridge offshore SW of Iceland. The Peninsula is formed of hyaloclastite ridges and basaltic lavas [39]. The oldest lavas on the surface are from the Late Pleistocene age while the youngest are from the Holocene [40]. Furthermore, the area is intensely fractured with normal faults and extension fractures,

within a narrow belt, along with eruptive fissures lying perpendicular to those extensional rifts [39,41]. There are four distinct volcanic systems on the Reykjanes Peninsula, from west to east: Reykjanes, Krísuvík, Brennisteinsfjöll, and Hengill fissure swarms [42,43], see Figure 1.

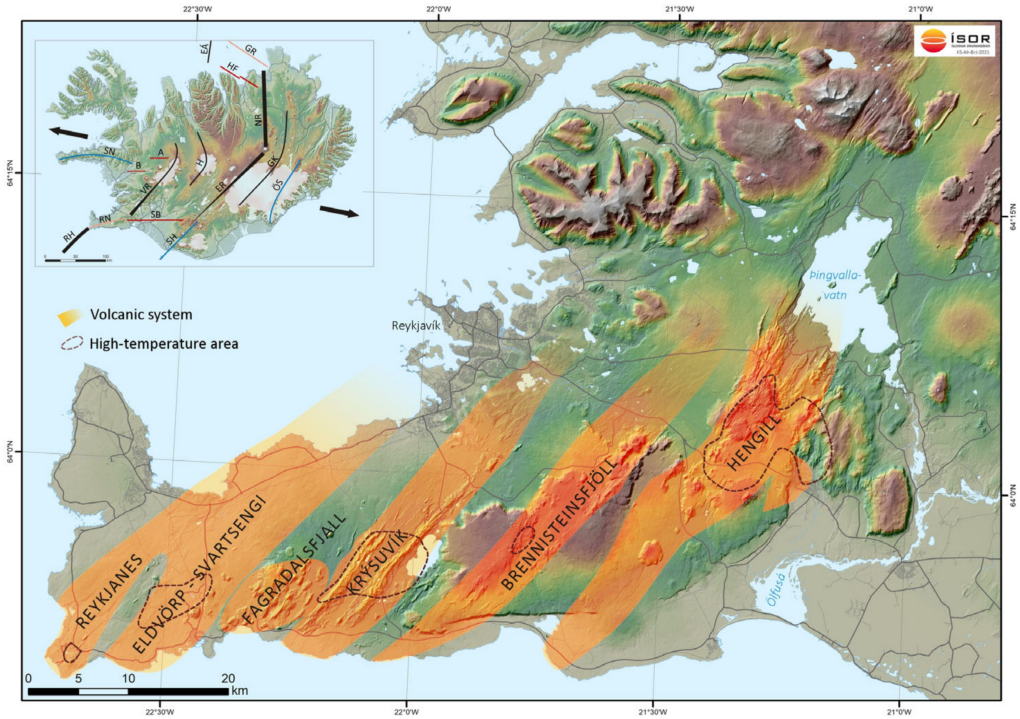

Figure 1. Geological map showing the location of the Reykjanes Peninsula and the fissure swarms in the area (image courtesy of Iceland GeoSurvey (ÍSOR)).

The Reykjanes fissure swarm, which the Reykjanes geothermal field is a part of, is at least 45 km in length, where 30 km are on land [44]. The Reykjanes geothermal field is at the SW tip of the Peninsula and is one of the smallest geothermal areas in Iceland. It is about 1–1.5 km^2, based on the geothermal features displayed on the surface [39]. The heat source of the Reykjanes geothermal field is thought to be dykes, thin sills, and/or a sheeted dyke complex. At a 5.5–6 km depth, a brittle-ductile transition marks the bottom of potential permeability, hence, the base of the hydrothermal system [45]. The chemical composition of the high-temperature hydrothermal fluid derives from the interaction of seawater with basaltic rocks made up mostly by hyaloclastite, volcanic breccias, and tuffaceous units to a depth of 1000 m [46]. Observations from the 2054 m deep well, RN-10, shows that at increased depths the stratigraphy consists predominantly of pillow basalts and formations exhibit relatively high porosity and low permeability with aquifers that are related to fractures along sub-vertical dyke intrusions [47]. The chemical composition of the liquid phase of the geothermal brine in well RN-29 at Reykjanes geothermal powerplant was measured by Iceland GeoSurvey (ÍSOR) in 2014 [48] and is shown in Table 1.

1.1.2. Chaunoy

The Keuper Triassic sediments were deposited during an extensional phase that induced the subsidence of the Paris basin [49]. The sediments were deposited in a continental environment, ranging from alluvial (west of the basin) to evaporitic (east of the basin) [50]. The maximum subsidence occurred east of Chaunoy while, to the west, the basin overlapped gently with the armorican variscan massif [51]. The Chaunoy reservoir is part of the Chaunoy sandstone, a Carnian-Norian lithostratigraphic formation due to a second-order Scythian-Carnian cycle of tectonic origin [52,53]. It lies conformably on reddish dolomitic shales deposited in a coastal plain [51]. The Chaunoy oil field (Figure 2A), located 50 km

south-east of Paris, is the largest oil field of the Paris basin [54]. It is a broad north-south anticline structure 15 km long and 5 km wide, with a faulted eastern flank [51,55]. The average thickness of the reservoir is approximately 66 m [51,55]. It developed in the distal part of alluvial deposits. Small ribbon channel deposits are interbedded with a flood plain and lacustrine deposits. The channel amalgamation occurred during periods of low accommodation, producing highly heterogeneous sand sheets [51]. During higher accommodation periods, channels became progressively isolated within flood plain mudstones. Finally, lacustrine mudstones were deposited, creating a vertical permeability barrier. Then, the decrease in accommodation induced a strong pedogenetic alteration responsible for dolocrete and groundwater dolomite. The amalgamation rate varied with cyclic lake-level variations, which directly controlled the reservoir geometry [51]. Due to this history, the reservoir is strongly heterogeneous. An upper siliciclastic/dolomitic member can be divided into two units with porous conglomeratic channels interfingered with cemented lagoonal dolomites. A lower siliciclastic member shows four heterogeneous sand sheets (7 m thick), which have been correlated across the field. Each of them is made up of stacked single channel sequences. The sand sheets are separated by extensive lacustrine and flood plain mudstone layers acting as permeability barriers. Bourquin et al. [56] presented a high-resolution sequence stratigraphy of the Chaunoy reservoir. The maximum net oil pay is 25 m with a 11 m average [51], in which the thickness of each reservoir unit ranges from 1 m to 5 m. In this field, the well spacing, 600 m in average, is larger than the channel width [51,54] which does not allow for a complete understanding either of the structure or of fluid flows as well-to-well correlations are hypothetical. The Liassic shales located directly above the Triassic reservoir constitute the oil source rock [51].

Table 1. Chemical composition of the liquid phase of well RN-29 at Reykjanes geothermal powerplant.

Analysis Year: 2014		
Chemical	**Value**	**Unit**
CO_2	45.5	mg/kg
H_2S	1.44	mg/kg
NH_3	2.06	mg/kg
B	13.1	mg/kg
SiO_2	1088	mg/kg
Na	14630	mg/kg
K	2520	mg/kg
Mg	2.86	mg/kg
Ca	1950	mg/kg
F	0.27	mg/kg
Cl	28600	mg/kg
SO_4	16.3	mg/kg
Al	0.022	mg/kg
Fe	3.82	mg/kg
Acidity	5.15	pH

The timing of the in-situ material exposure performed at Chaunoy oil field coincided with an ORC powerplant demonstration performed within the framework of the MEET project. Exhaust water coming out of the CNY40 oil well (Figure 2B) was connected to the inlet of an ORC powerplant. The samples tested in this work at Chaunoy were placed within the exhaust water flowline (Figure 2C) connected to the inlet of the small-scale ORC unit (Figure 2D). The cooled water coming out of the ORC was reinjected with the whole exhaust flow. The oil field showed a high water cut with approximately 96 L of water for every 1 L of oil produced (Vermilion, personal communication).

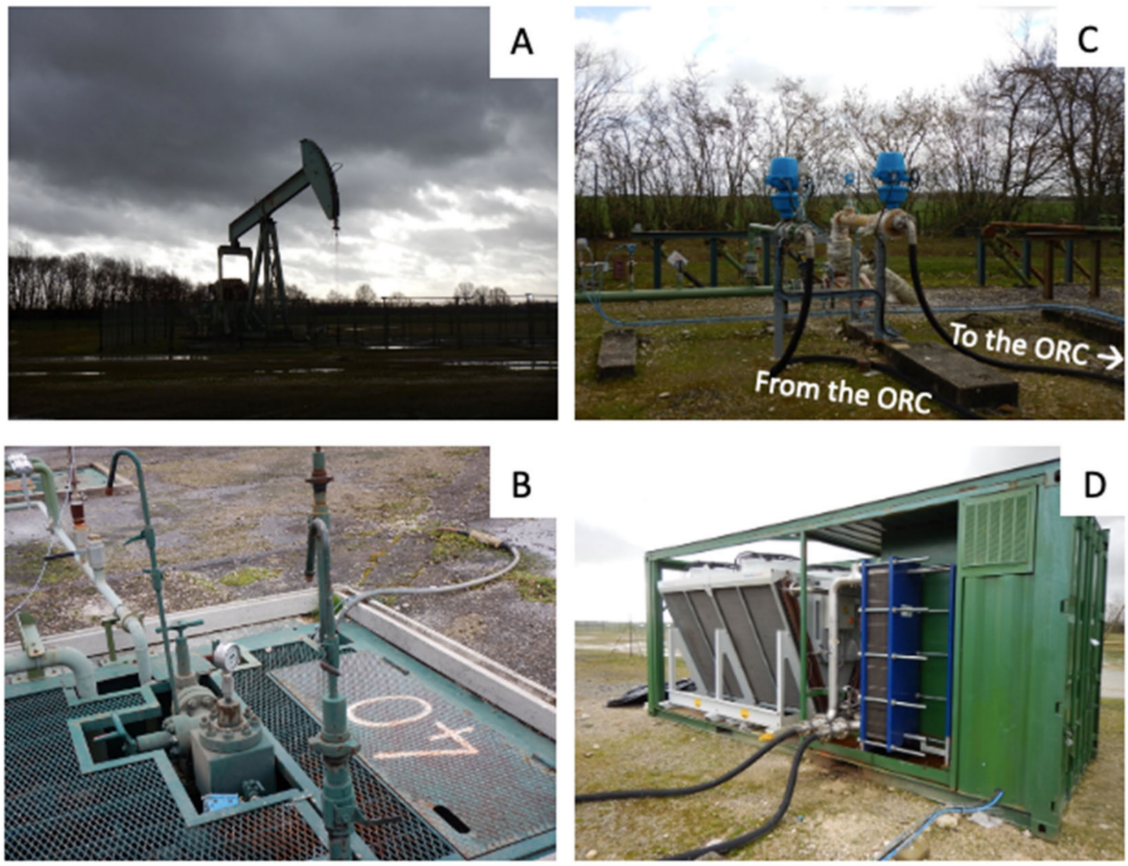

Figure 2. The small-scale mobile Organic Rankine Cycle (ORC) unit installed at Chaunoy oil field. (**A**): one of the oil wellheads, (**B**): head of the CNY40 well from which the oil and hot water are extracted, (**C**): the connection of the hot water pipe to the ORC unit, (**D**): the mobile ORC unit connected to the water pipe. The samples tested at Chaunoy in this work were placed within the inlet of the ORC unit during a 4-month demonstration.

2. Materials and Methods

The corrosion experiments were based on the Standard Guide for Conducting Corrosion Tests in Field Applications, ASTM-G4-1 [4]. The corrosion experiments were conducted by exposing the four potential heat exchanger materials in the form of metal coupons at the two locations: Reykjanes and Chaunoy. The coupons were placed on a sample holder, with ceramic isolation rings to avoid the electrical contact between the holder and the coupon samples. The sample holder was placed in a pressure vessel for Reykjanes and in a flow-line pipe for Chaunoy. The 254SMO was bought from Outokumpu, Inconel 625 was bought from ThyssenKrupp, 316L was bought from Outokumpu and Stálnaust, and Ti gr. 2 was acquired from The Welding Institute (TWI). The dimensions of the coupons were in all cases 50 × 25 × 3 mm except for Ti gr. 2 which was 4 mm in thickness. The elemental compositions of the materials tested are shown in Table 2.

2.1. Reykjanes

The coupon samples were exposed inside a pressure vessel at Reykjanes, seen in Figure 3, for 30 days. The temperature and pressure were 200 °C and 18 bar, respectively. The fluid in the pressure vessel was saturated with geothermal steam which had already passed through a separator. The gas concentrations of the steam present in the pressure vessel, which is the same steam as is fed to the turbines of the Reykjanes power plant, can be seen in Table 3.

Table 2. Elemental composition of the materials tested in this work.

	Material			
Element (% wt.)	**316L**	**Inconel 625**	**254SMO**	**Ti gr. 2**
C	0.02	-	-	0.08
Si	0.5	0.2	0.4	-
Mn	1.0	0.1	0.7	-
Fe	Balance	4.5	Balance	0.3
Ni	10.1	Balance	17.8	-
Mo	2.0	6.7	6.1	-
Cr	17.1	21.4	19.8	-
Cu	-	-	0.3	-
N	0.04	-	0.3	0.03
Ti	-	0.2	-	Balance
Nb	-	3.4	-	-
H	-	-	-	0.015
O	-	-	-	0.025

Figure 3. The coupons being removed from the pressure vessel at Reykjanes power plant where they were exposed.

Table 3. Gas concentrations in the pressure vessel at Reykjanes power plant [57].

Chemical	**Value**	**Unit**
CO_2	6600	mg/kg
H_2S	220	mg/kg
H_2	1.9	mg/kg
N_2	66	mg/kg
CH_4	0.9	mg/kg

2.2. Chaunoy

The Chaunoy oil field is in the Paris basin, in northern France, where the salinity is around 6.5 wt.%. The fluid from the tested oil well is mostly hot geothermal water, with a

small amount of oil. The test was conducted by placing the coupons on a sample holder rack, which was placed inside a flowline at the inlet of an ORC power production unit. The sample rack before and after testing can be seen in Figure 4.

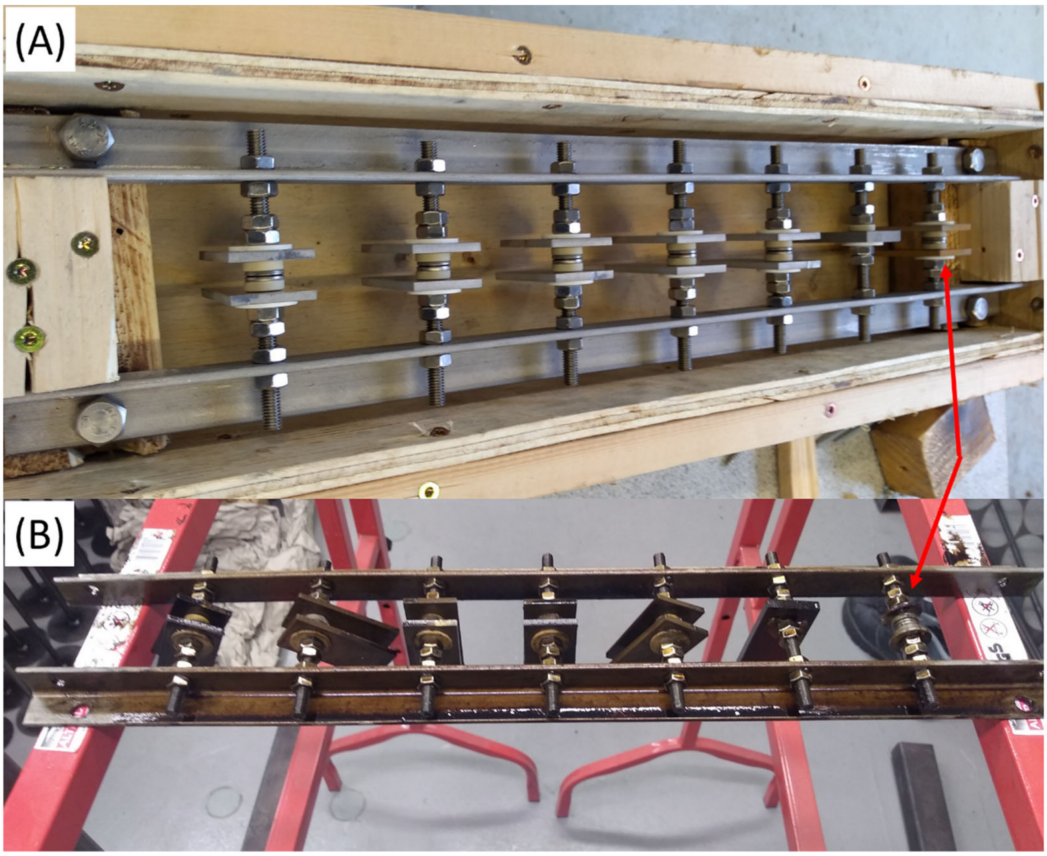

Figure 4. (**A**): The samples on a rack which was inserted into an oil flowline at Chaunoy. (**B**): The rack and samples after testing had been conducted. It is interesting to note that two carbon steel coupons, which are not investigated in this work, had corroded severely, and fallen off of the threaded rod during exposure as marked with red arrows.

The Chaunoy exposure was conducted in well CNY40 for four months. The temperature at the wellhead was measured at 94 °C, the oil ratio of the fluid was 1.85%, and the flow rate was 6.25 l/s. The pressure was on average 9.5 bar. A chemical analysis of the fluid can be seen in Table 4.

Table 4. Chemical analysis of the fluid in well CNY40.

Analysis Year: 2009		
Chemical	**Value**	**Unit**
Ba	2.82	mg/L
Ca	3986	mg/L
Fe	1.6	mg/L
Mg	572.7	mg/L
Mn	0.29	mg/L
Na	22910	mg/L
Sr	297.8	mg/L
K	572.8	mg/L
Cl^-	41967	mg/L
S	399	mg/L
HCO_3^-	1696.1	mg/L
Acidity	7.15	pH

2.3. Material Assessment

The samples were analysed both topographically and cross-sectionally using an optical microscope, AXIO from Zeiss, and a Scanning Electron Microscope (SEM), Supra 25. A chemical analysis was conducted using an Energy-Dispersive X-ray spectroscopy (EDX) detector, Oxford Instrument X-max. For simplicity, the analysis was only given for elements over 0.5 wt.%.

The samples were dismounted from the racks and photocopied with Canon MG5450 before assessment. The Backscatter Electron (BSE) detector of the SEM was used for the topography imaging and a secondary detector was used for cross-section imaging. The cross-sections were prepared by cutting the samples with a diamond cutter and baking in conductive phenolic epoxy for 3.5 min at 150 °C. The samples were polished in steps until reaching 1 µm roughness. The macro and micro-structure images were taken at the most affected areas with a good distance from the edges to avoid artifacts from surface preparation. For the EDX analysis, the cross-section might contain C and O contamination from sample preparation and handling as well as from the vacuum chamber of the SEM.

3. Results and Discussion

3.1. Material Evaluation

Visual appearance is the first indicator of material performance after exposure and the photocopied samples can be seen in Figure 5. Where the coupons were fastened to the rack, marked with a red circle, there was an area which was masked, sometimes partially, from the geothermal environment. Utilising masked areas as a reference in corrosion exposure has been reported [58]. The difference in surface appearance between the exposed areas compared to the masked areas was evident for 316L, 254SMO, and Ti gr. 2 tested at Reykjanes. It is important to note, due to the testing set-up, that only the area, marked with a blue box, of Ti gr. 2 was exposed. Inconel 625 did not show visible discoloration after being exposed at Reykjanes. The discoloration formed at the surface of the 316L, 254SMO, and Ti samples tested at Reykjanes was well adhering. The samples exposed at Chaunoy had an indication of fluid deposits where layers had loosely formed on the surfaces of the samples with low adherence.

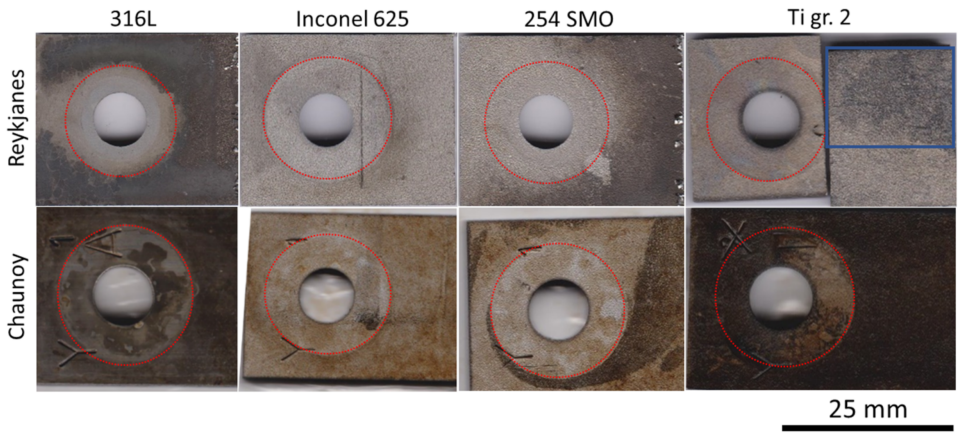

Figure 5. Coupons after exposure, the sample size is 25 mm in the vertical direction. The red circles indicate the covered areas, unexposed, due to ceramic shielding of the fastener. The blue square on the Ti gr. 2 sample exposed in Reykjanes marks the main affected area of the sample. The samples exposed in Reykjanes showed discoloration on all samples except the Inconel 625. The samples exposed in Chaunoy showed an indication of deposits from the fluid for all samples.

The macroscopic topography evaluation of the tested samples gave an indication of the general surface texture of the samples which can be seen in Figure 6, where high roughness is evident for 254SMO and Inconel 625. There was a surface texture difference within 316L exposed at different locations which might partly be due to a different provider.

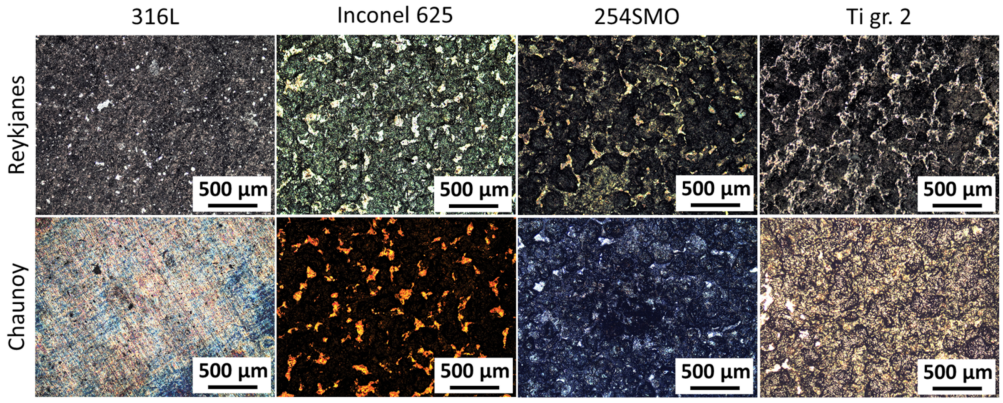

Figure 6. Optical topography images where the above line has the samples tested in Reykjanes and below are the samples tested in Chaunoy.

Topography images taken with the BSE detector are shown in Figure 7, where the 316L had microscopic defects at the surface both when tested in Reykjanes and Chaunoy. Inconel 625 and 254SMO had high surface roughness. Furthermore, there was a pit present at the surface of 254SMO exposed at Reykjanes. The topography microstructure indicated erosion in the Ti gr. 2 both tested at Reykjanes and Chaunoy where valleys are present. Furthermore, there were Fe-S rich deposits at the surface. Similar deposits have been reported for Ti in supercritical geothermal environments [59]. The microstructure analyses of the surfaces demonstrated point defects on 316L, micro-roughness on Inconel 625, defect on 254SMO, and Ti gr. 2 showed an indication of erosion.

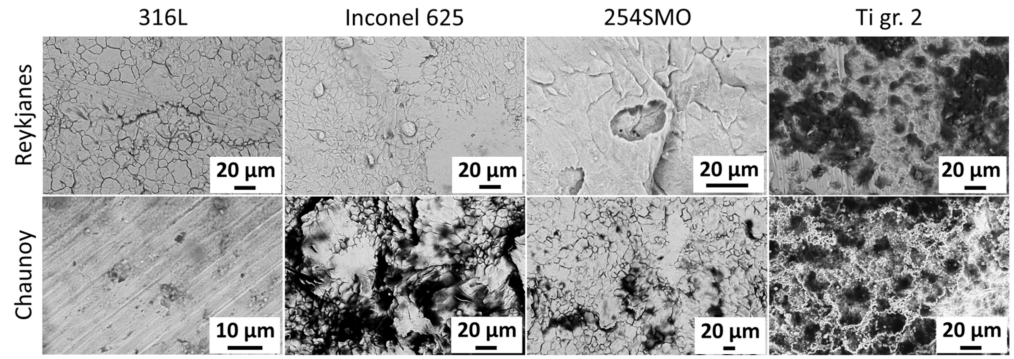

Figure 7. Topography images taken with Backscatter Electron (BSE) detector of the surfaces of the exposed coupons.

Similar to the topography images, seen in Figure 7, the microscopic cross-sectional images, seen in Figure 8, contained micro roughness for 254SMO and Inconel 625. The 316L tested at Chaunoy had a smooth surface with a defect of around 5 µm into the subsurface containing corrosion deposits. The Reykjanes-exposed 316L sample had unhomogenized corrosion layers covering the surface. The 254SMO had subsurface cracks after exposure in Reykjanes and Chaunoy while Inconel 625 had subsurface cracks only for samples tested in Chaunoy. Both 254SMO and Inconel 625 contained high amounts of Ni and Mo. Furthermore, there was the presence of inclusions within both materials contributing to weak areas.

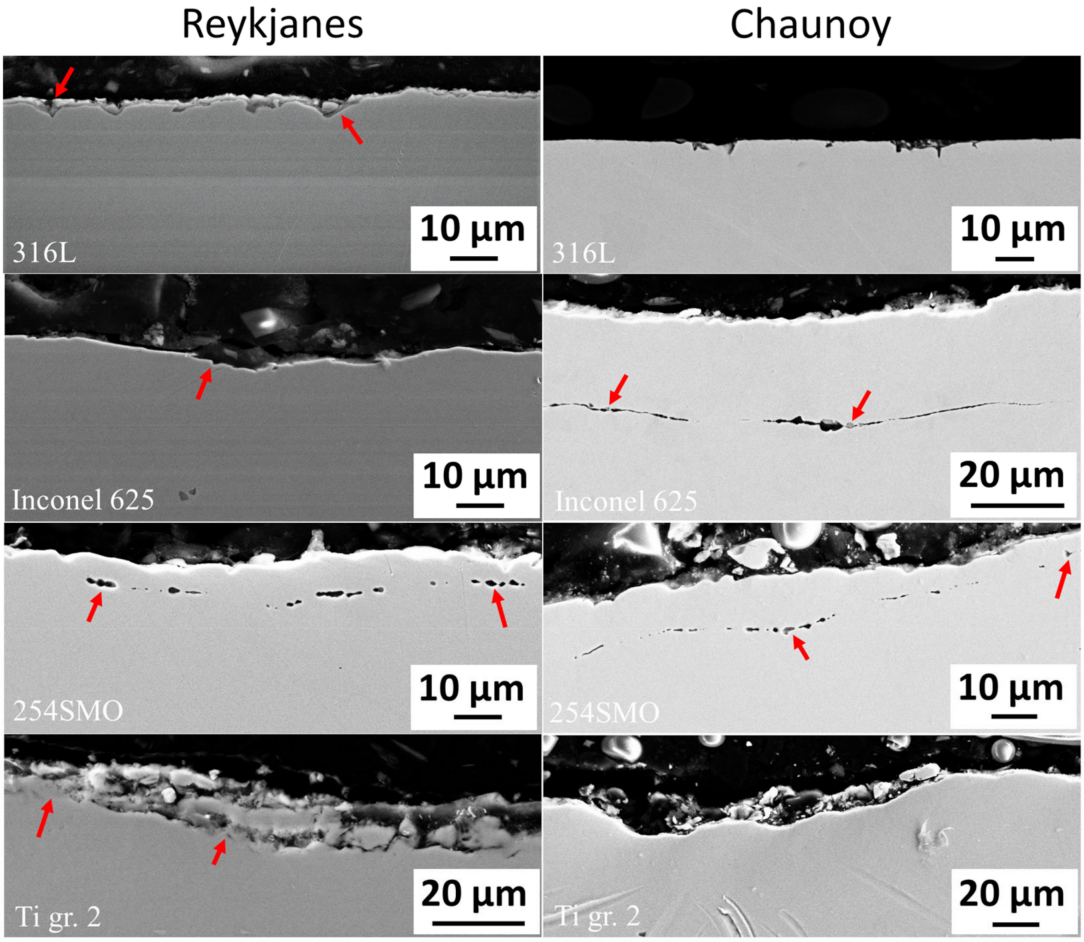

Figure 8. Scanning Electron Microscope (SEM) cross-section images taken of the most affected areas detected after exposure in both locations. The arrows indicate areas of interest: corrosion layer for 316L (Reykjanes), subsurface cracks for Inconel 625 (Chaunoy) and 254SMO (Chaunoy and Reykjanes), and abrasion of Ti gr. 2 surfaces (Chaunoy and Reykjanes).

3.2. Material Characterisation

The results from the microstructural analysis are detailed in the section below. The chemical composition of the bulk material for reference is included in the material characterisation.

3.2.1. Austenitic Stainless Steel—316L

The 316L is one of the most commonly used materials in the geothermal environment [29]. Figure 9 shows the cross-section of 316L where two corrosion layers are present along the profile. The estimated pH level of the environment was 5 at Reykjanes, which is an unstable state for Cr. The inner corrosion layer marked 1, 2, and 5 in Figure 9 consisted of high Cr/Fe and Mo/Fe ratios of 0.51–0.76 and 0.05–0.07 respectively. The measured reference ratio of Cr/Fe and Mo/Fe for bulk material was 0.26 and 0.03, respectively. The outer corrosion layer marked 3, and 4 consisted mostly of Fe and O products. The elemental analysis of the locations in the figure is detailed in Table 5. This finding is in line with 316L tested in an H_2S environment where the inner layer is Cr and Mo rich and the outer layer has Fe segregation measured at pH 4 [60].

Unlike after exposure in Reykjanes, the 316L after exposure in Chaunoy, which had a pH level of 7, did not show the same corrosion layer formation. However, there were local defects scattered over the surface as seen in the topography image in Figure 10A. Furthermore, defects were seen in the cross-section images, Figure 10B. The elemental analysis of locations shown in Figure 10A is detailed in Table 6. There were traces of S and Si from the exposure found within corrosion deposits at the defects. The deposits

mainly consisted of Fe, O, and Cr. Traces of Al were found, which can be a typical inclusion material in stainless steels [61].

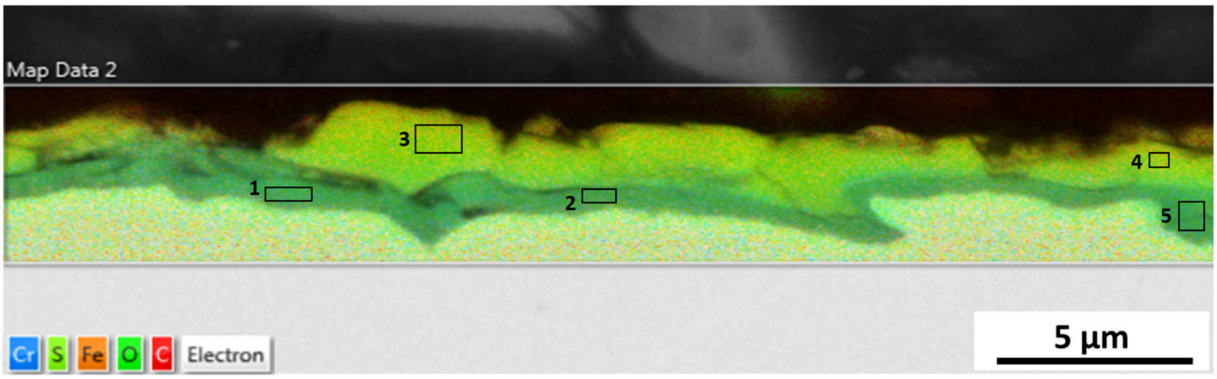

Figure 9. Elemental analysis and mapping of 316L after being exposed in the pressure vessel at Reykjanes at 200 °C, showing locations where Energy-Dispersive X-ray spectroscopy (EDX) elemental analysis was performed. There are two semi-homogenous layers over all the cross-sections analysed. The layer in locations 1, 2 and 5 is an inner corrosion layer while the top layer, locations 3 and 4, is an outer corrosion layer mostly composed of Fe and O. The colour map shows the relative composition of Cr, S, Fe, O and C in the material.

Table 5. EDX elemental analysis of locations shown in Figure 9. For comparison, an analysis of the bulk material after Reykjanes exposure is included.

	Location					
Element (wt. %)	**1**	**2**	**3**	**4**	**5**	**Bulk**
C	20.5	8.8	27.2	27.6	6.8	5.0
O	22.6	19.0	26.6	23.9	19.5	-
Si	0.7	0.7	0.5	0.3	0.8	0.60
S	2.3	3.5	0.6	2.1	3.9	-
Cr	18.2	18.7	1.4	3.2	20.9	16.8
Fe	23.8	37.0	43.2	38.5	34.8	65.8
Ni	6.1	8.2	-	2.6	8.3	9.6
Mo	1.7	1.8	-	0.9	2.2	2.1
Ba	2.5	2.2	-	0.4	2.5	-

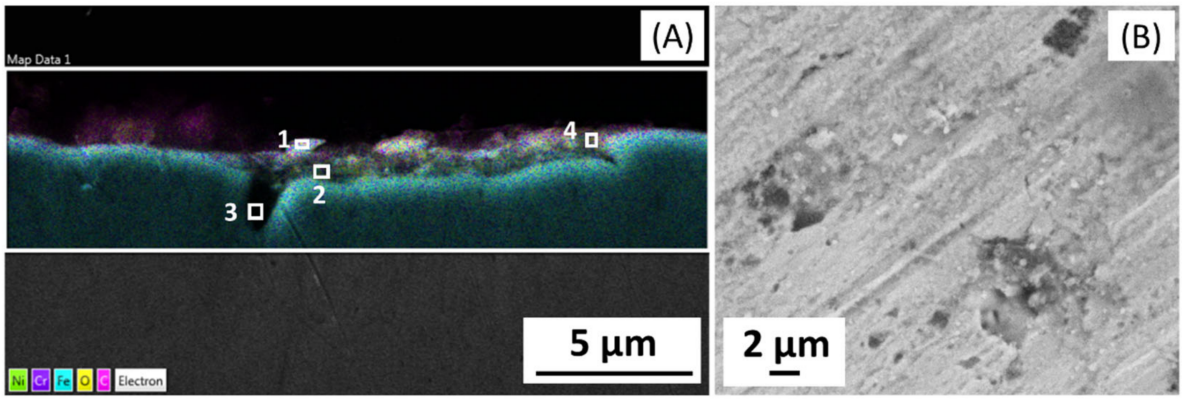

Figure 10. EDX elemental analysis of 316L after exposure in Chaunoy. (**A**): Cross-sectional elemental mapping of a surface defect, where locations marked for EDX elemental analysis are shown. Location 3 is inside the small surface defect, while locations 1, 2 and 4 are corrosion deposits around the defect. The colour map shows the relative elemental composition of Ni, Cr, Fe, O and C in the image. (**B**): Topography image of the surface defect by SEM.

Table 6. EDX elemental analysis of locations shown in Figure 10A.

	Location				
Element (wt. %)	**1**	**2**	**3**	**4**	**Bulk**
C	69.2	39.5	6.0	49.8	4.7
O	11.1	13.0	-	16.8	-
Al	0.7	1.0	-	0.9	-
Si	1.1	1.7	-	1.3	0.4
S	0.8	2.0	-	1.9	-
Ca	1.6	0.8	0.2	0.8	-
Cr	2.9	7.3	16.2	5.7	16.8
Fe	10.4	29.6	65.6	18.7	66.7
Ni	1.4	3.9	9.7	3.3	9.9
Mo	-	-	1.5	-	1.6

3.2.2. Nickel Alloy—Inconel 625

Inconel 625 is a Ni-alloy used within the geothermal sector and is recommended for sulphur rich environments [62]. Figure 11 shows locations of the chemical and microstructural analysis of Inconel 625 after exposure in Reykjanes. Table 7 details the chemical analysis of the locations analysed in the figure. A horizontal crack was detected within the material after exposure. The crack contained O and a high ratio of Cr/Ni was measured at 1.4–1.8 while the base material had a ratio of 0.3. Furthermore, the Mo/Ni ratio was slightly higher in the crack. The results indicate that when the crack is formed, Cr and Mo will diffuse into the crack and together with oxygen seal it. A trace of S was also found within the crack. The surface seemed to be unaffected by the exposure which is reflected in Figure 5 where the exposed sample contains a similar appearance to the masked area.

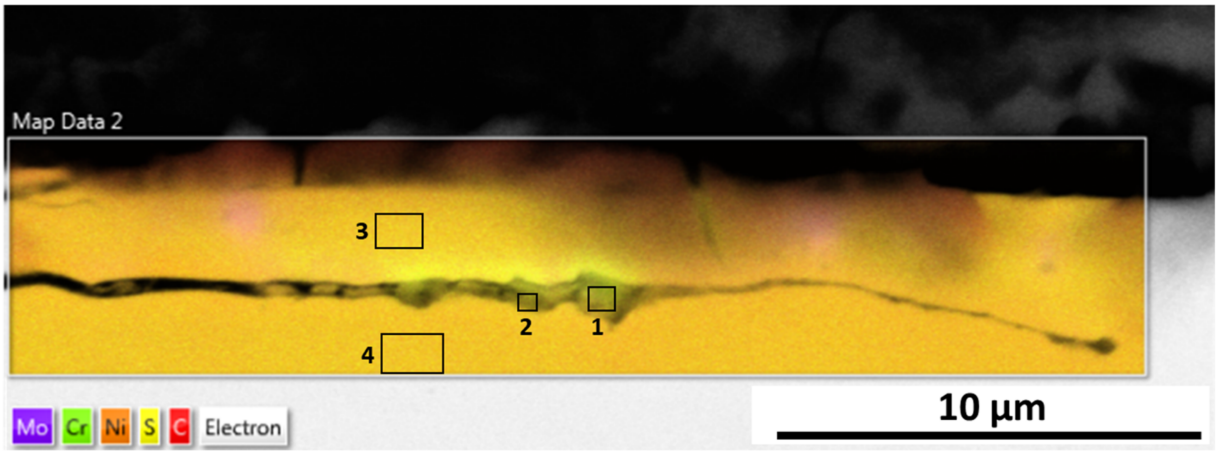

Figure 11. Elemental mapping and EDX analysis of Inconel 625 exposed in Reykjanes, which showed crack propagation that might have initiated from inclusions as a high amount of Nb is present in location 1. Nb carbides are commonly found inclusions within Inconel 625 [63]. The measured area within the crack shows traces of S in locations 1 and 2. The colour map shows the relative composition of Mo, Cr, Ni, S and C in the material.

The Inconel 625 exposed in Chaunoy contained subsurface cracks parallel to the surface which crossed the inclusions as seen in Figure 12. Due to geometric discontinuity, the inclusions often act as weak points in materials [34] and can be prone to cracking and crack propagation.

Table 7. EDX elemental analysis of locations shown in Figure 11. For comparison, an analysis of the bulk material after exposure at Reykjanes is included.

	Location				
Element (wt. %)	**1**	**2**	**3**	**4**	**Bulk**
C	9.1	7.0	12.8	8.7	8.6
F	-	-	4.0	3.3	-
O	20.7	15.2	-	-	-
S	2.3	4.4	-	-	-
Cr	36.6	38.0	16.4	16.1	16.4
Fe	2.3	2.2	3.7	3.9	4.1
Ni	20.1	26.6	53.3	58.6	61.3
Nb	5.6	2.5	2.5	2.2	-
Mo	2.4	3.2	6.9	6.9	7.1

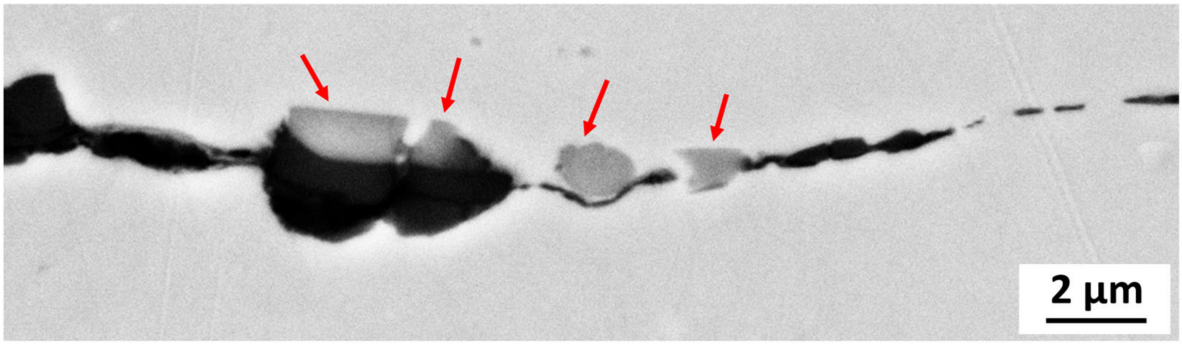

Figure 12. SEM cross-sectional image of the Inconel 625 after exposure in Chaunoy where inclusions are seen within crack propagation, marked with arrows.

Microstructural analysis of another crack propagation within the Chaunoy-exposed Inconel 625 can be seen in Figure 13. The Cr/Ni and Mo/Ni ratios were 0.26–0.3 and 0.1–0.12, respectively, in bulk material and within cracks where the inclusions were present as seen in Table 8. Similar ratio was found within the bulk material of the Reykjanes-exposed samples. The pH level of the environment was 7 which indicates a passive state of Cr and Mo, resulting in poor mobility for the elements to diffuse into the crack and seal it.

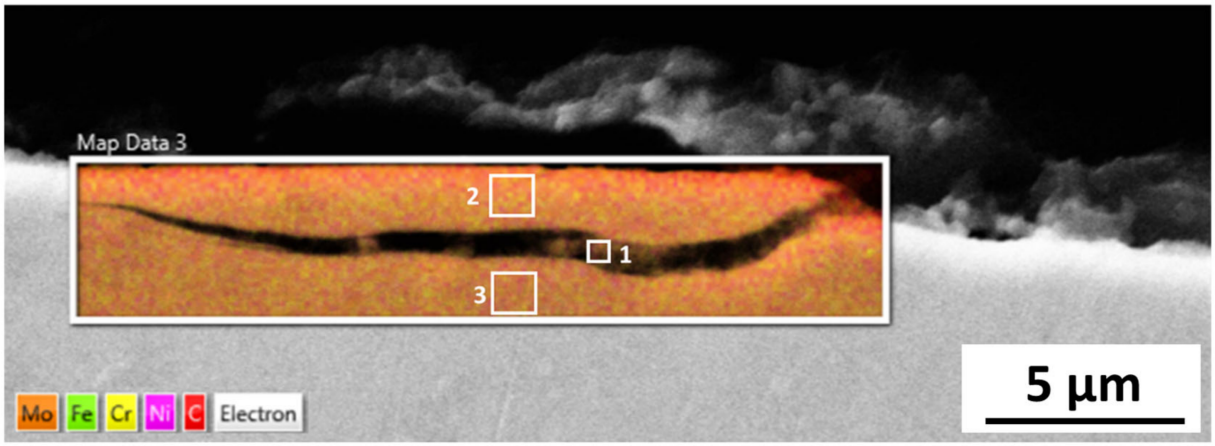

Figure 13. Microstructural analysis of Chaunoy-exposed Inconel 625 taken with SEM, where inclusions are seen within crack propagation in location 1. The colour map shows the relative composition of Mo, Fe, Cr, Ni and C in the material.

Table 8. EDX elemental analysis of locations shown in Figure 13. For comparison, an analysis of the bulk material after exposure at Chaunoy is included.

	Location			
Element (wt. %)	**1**	**2**	**3**	**Bulk**
C	13.4	28.8	8.6	7.5
O	3.9	2.6	0.8	-
Cr	14.6	12.4	16.3	18.2
Fe	3.8	3.0	4.1	4.0
Ni	55.8	46.0	60.1	60.5
Nb	1.5	1.3	2.1	2.2
Mo	5.6	4.7	7.0	7.4

The crack propagation from the weak inclusion areas could be due to the brittleness of the alloy when exposed to rapid temperature changes. From Figure 5, and the microscopic analysis, there is little to no evidence of corrosion taking place at the surface.

3.2.3. Super Austenitic Stainless Steel 254SMO

The 254SMO is a super austenitic stainless steel, which contains high amounts of alloying elements Cr, Ni, and Mo. Furthermore, 254SMO has shown good performance in acidic [33] and sea water environments [21]. The cross-section of 254SMO and topography after exposure in Reykjanes can be seen in Figure 14. The topography image shows the typical surface texture found over the surface of the sample after being exposed at Reykjanes. Furthermore, contamination was present at the surface. The cross-section shows voids at the subsurface in close proximity to grooves at the external surface. These voids contained O and S as can be seen from Table 9.

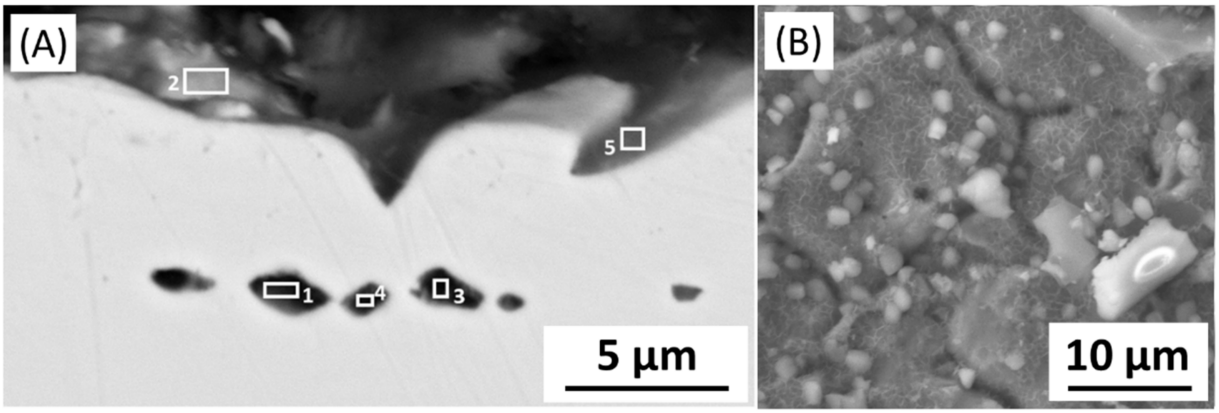

Figure 14. The 254SMO after exposure in Reykjanes taken with BSE detector (**A**): Cross-sectional SEM of the surface of the sample showing locations elementally analysed. (**B**): Topography SEM image of the 254SMO after exposure at Reykjanes.

A pit was found on the surface of the material after testing in Reykjanes as seen in Figure 15A. Due to the naturally formed passivation layer on the 254SMO surface, pits grow under the surface layer [64]. The cross-section, in Figure 15B, shows a crack propagation at the subsurface which led to the breaking of the material causing direct exposure of the metal which could result in pit formation as seen in Figure 15A.

Table 9. EDX elemental analysis of locations shown in Figure 14. For comparison, an analysis of the bulk material after exposure at Reykjanes is included.

	Location					
Element (wt. %)	**1**	**2**	**3**	**4**	**5**	**Bulk**
C	13.3	49.1	36.9	32.1	46.0	6.1
O	5.7	-	4.4	3.5	10.1	-
Al	-	3.6	-	-	-	-
S	1.1	0.8	0.6	-	0.9	-
Ca	4.6	0.6	3.3	2.5	0.7	-
Cr	18.1	9.0	12.7	13.5	7.9	19.5
Fe	44.5	28.8	31.6	35.1	23.6	50.4
Ni	12.0	7.5	8.5	9.8	7.5	17.0
Cu	-	0.6	-	-	-	0.8
Mo	-	-	1.5	2.3	1.4	5.6

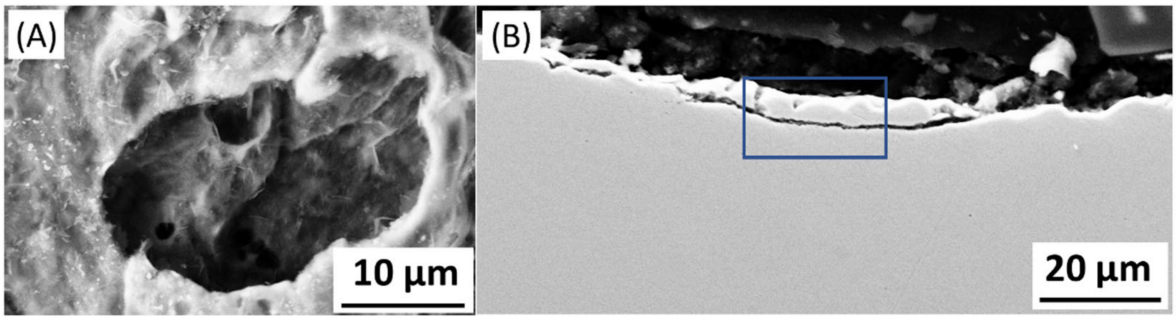

Figure 15. 254SMO microstructural analysis using secondary detector (SEM) from Reykjanes exposed sample (**A**): Pit found at the surfaces of the 254SMO. (**B**): Cross-section where a sub-crack is present. The area marked in blue is further analysed in Figure 16.

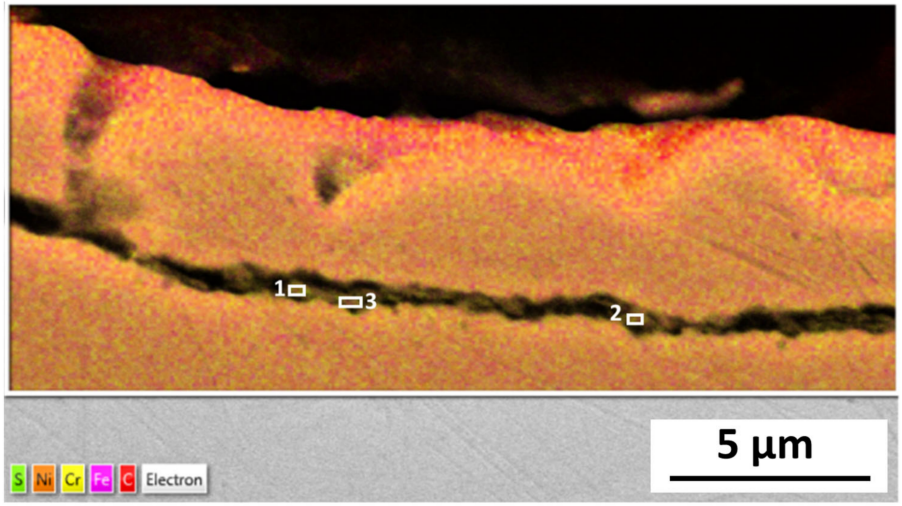

Figure 16. Elemental mapping of within the subsurface crack propagation of 254SMO after Reykjanes exposure, showing the locations of EDX elemental analysis inside the crack. The colour map details the relative elemental composition of S, Ni, Cr, Fe and C in the material.

Higher magnification of the crack in the area marked with blue in Figure 15B, is shown in Figure 16 and an elemental analysis of locations in the crack is presented in Table 10. Within the crack was a high ratio of Cr/Fe, or 0.6–0.8, compared with the bulk material and voids at the subsurface with around 0.4 Cr/Fe ratio. Like Inconel 625, the Cr could have diffused from the bulk material forming the thin layer where the pH level was 5. There was a high wt.% ratio of O/Fe within the crack of 0.4–0.6. The Cr rich layer in the crack

seemed to be brittle, and part of the material was breaking off at places. The 254SMO might contain weak areas due to inclusion and increased brittle areas due to high wt.% of Mo [31]. The practical environment could promote crack propagation from weak areas resulting in material thinning.

Table 10. EDX elemental analysis of locations shown in Figure 16. For comparison, an analysis of the bulk material after exposure at Reykjanes is included.

	Location			
Element (wt. %)	**1**	**2**	**3**	**Bulk**
C	13.0	10.0	12.1	6.2
O	17.5	14.1	15.1	-
Al	0.9	1.1	1.2	-
S	0.9	1.1	1.2	-
Cr	23.4	21.4	22.5	19.5
Mn	2.7	3.1	2.6	-
Fe	29.8	35.2	33.6	50.4
Ni	8.5	10.7	8.3	17.0
Cu	-	-	0.6	0.8
Mo	3.0	4.1	3.2	5.6

The sample exposed in Chaunoy, seen in Figure 17, had a crack forming parallel to the surface of 254SMO. Between the detachment layer and the 254SMO there were both inclusion elements such as Al and Si as well as elements from the fluid such as Cl, Ca, Na, and S as seen in Table 11.

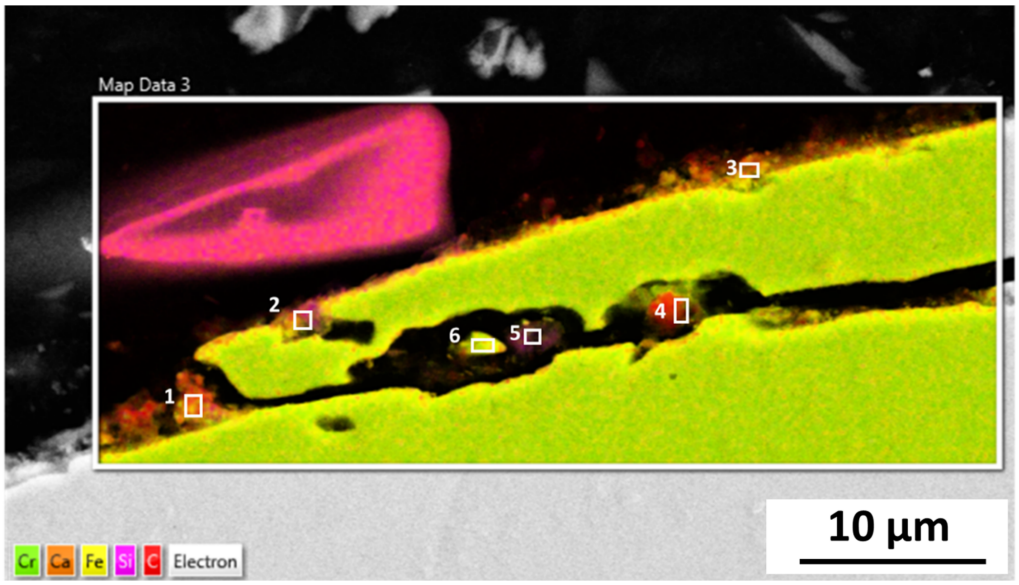

Figure 17. Element mapping and analysis of 254SMO after being exposed in Chaunoy. Within the crack there is visible inclusion of Al and Si, number 5. Furthermore, there is corrosion deposit in locations number 1, 2, and 3, containing S and elements from the base material, Cr, Fe, and Ni. The colour map shows the relative chemical composition of Cr, Ca, Fe, Si and C in the material.

3.2.4. Titanium Grade 2

Ti gr. 2 is commercially pure, and is often preferred where high specific strength is needed [65]. The Ti gr. 2 naturally forms a TiO_2 passivation layer of a few nm which protects the bulk material. However, due to the low thickness of the TiO_2 passivation layer it can easily erode during exposure from the high velocity fluid which can contain abrasive particles. Figure 18 shows the sample after exposure where the affected area is evident. There were parallel subsurface cracks where the metal was adhering in a few contact points.

The EDX revealed Cu deposits, which can be found at Reykjanes [66]. The cross-section clearly supports the observation of the topography, from Figure 7, where erosion has taken place at the surface as can be seen in Figure 18. The EDX analysis performed in between the loosely adhering Ti contained high wt.% of O and C, presented in Table 12. Due to the position of the point evaluation, it cannot be excluded that phenolic epoxy, the sample mounting material, contributed to the signal from C and O. The Ti gr. 2 has been reported to be successfully used in an oxygen rich environment [67–69]. However, in geothermal environments, where free O is limited, a Ti alloy might be better suitable.

Table 11. EDX elemental analysis of locations shown in Figure 17. For comparison, an analysis of the bulk material after exposure at Chaunoy is included.

	Location						
Element (wt. %)	**1**	**2**	**3**	**4**	**5**	**6**	**Bulk**
C	54.0	35.3	59.0	81.6	29.6	35.9	6.8
O	10.1	15.5	5.7	3.0	28.2	3.9	-
Na	2.5	1.6	0.8	3.2	5.0	3.7	-
Al	0.3	1.6	0.1	-	3.8	0.2	-
Si	0.6	3.5	0.2	0.1	10.5	0.5	0.5
P	0.5	0.2	0.6	-	-	0.1	-
S	6.6	7.8	6.3	0.4	1.5	0.8	-
Cl	2.7	0.5	0.7	2.5	1.4	3.1	-
Ca	1.9	1.1	1.8	0.3	1.0	0.6	-
Cr	2.2	3.0	2.8	2.0	4.2	10.3	19.4
Fe	15.9	25.0	18.4	5.5	12.4	29.1	50.1
Ni	1.5	2.6	2.3	1.2	2.3	9.1	16.7
Cu	0.2	-	-	-	-	-	0.7
Mo	-	0.9	-	-	-	2.2	5.8
Ti	-	-	0.7	-	-	-	-

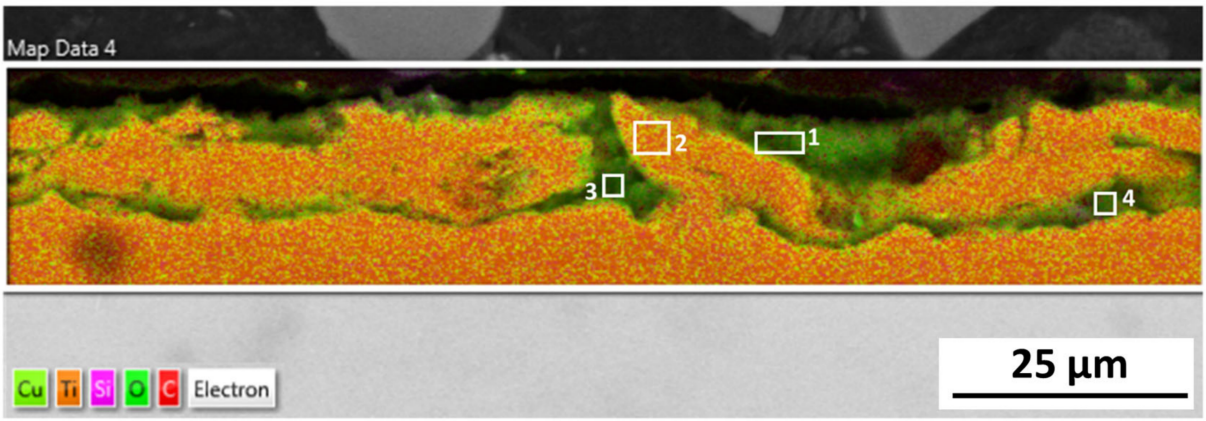

Figure 18. Ti gr. 2 after exposure in Reykjanes where around 10 µm of material is loosely attached to the base material. Four locations analysed with EDX are shown. Locations 1,3 and 4 show high amounts of Cu deposits while location 2 is nearly pure Ti. The profile shows an indication of erosion. The colour map shows the relative composition of Cu, Ti, Si, O and C in the material.

The Ti gr. 2 tested in Chaunoy, seen in Figure 6, showed an indication of erosion at the surface which is further supported with topography images. Figure 19 shows the affected area where Ti was eroding and a 10 µm metal part was loosely adhering to the surface along with S-Fe rich corrosion products. Table 13 details the elemental analysis of locations shown in the figure.

Table 12. EDX elemental analysis of locations shown in Figure 18. For comparison, an analysis of the bulk material after exposure at Reykjanes is included.

	Location				
Element (wt. %)	**1**	**2**	**3**	**4**	**Bulk**
C	49.1	4.0	45.6	39.3	2.5
O	21.4	-	19.8	15.3	2.5
Ca	0.3	-	1.0	0.7	-
Ti	5.1	95.0	7.0	24.7	94.9
Fe	1.2	0.2	0.7	0.9	0.1
Cu	21.2	0.3	24.8	18.5	-

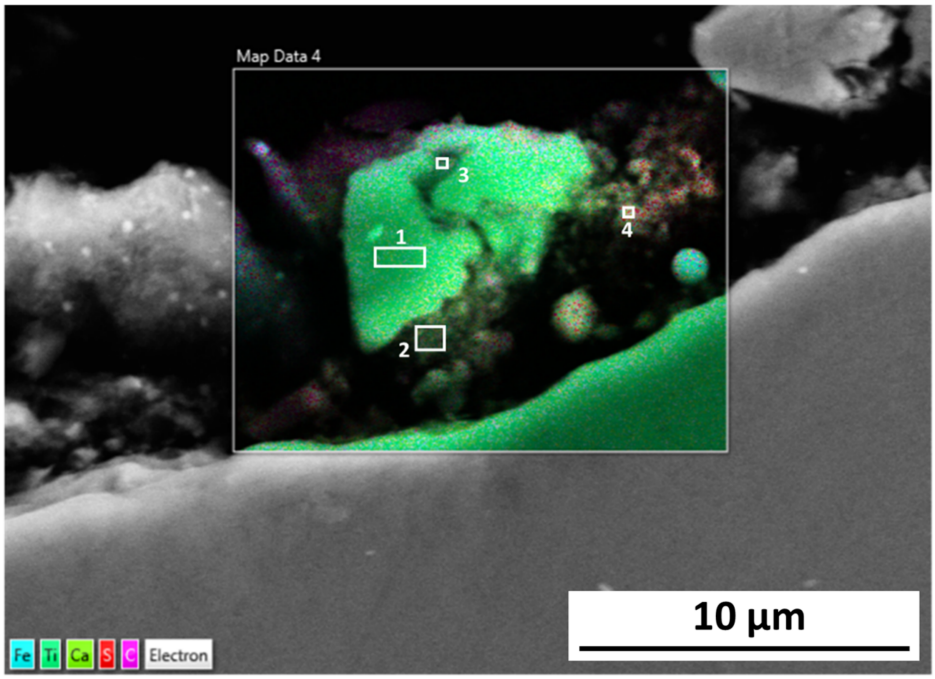

Figure 19. Ti gr. 2 after exposure at Chaunoy where there is visible detachment of Ti subsurface. The detached material is seen in location number 1. Furthermore, locations 2 and 4 contain Ti with high amounts of Fe and S. The colour map shows the relative composition of Fe, Ti, Ca, S and C in the material.

Table 13. EDX elemental analysis of locations shown in Figure 19. For comparison, an analysis of the bulk material after exposure at Chaunoy is included.

	Location				
Element (wt. %)	**1**	**2**	**3**	**4**	**Bulk**
C	4.3	21.3	28.4	38.2	2.2
O	6.8	11.6	10.5	8.3	3.9
Si	-	0.7	0.5	0.3	0.1
S	0.2	11.4	1.5	16.3	-
Ca	0.4	1.2	0.9	1.7	0.1
Ti	87.9	34.7	52.6	5.9	93.6
Cr	-	-	4.6	0.5	-
Fe	0.4	18.7	-	28.5	-

4. Conclusions

The most accurate method for evaluating the material performance for a geothermal application is with direct exposure of the material in the geothermal environment. Such

experiments give an important indication of the viability of engineering materials in the particular geothermal setting in order to ensure the sustainability of geothermal projects. The material exposure is dependent on fluid parameters such as the ratio between steam and liquid form, corrosive ions and gases, temperature, and pressure. Furthermore, the abrasiveness of particles found within the fluid coming from the underground or high fluid velocity can also affect the material.

While the two geothermal locations differ widely in geological setting, they have some similarities when it comes to geochemistry. Both geothermal fluids, at the wellhead, have high salinity and calcium content. However, the fluid in Reykjanes is quite a bit more acidic when compared to the Chaunoy fluid, and while Reykjanes holds a high amount of SiO_2, the fluid at Chaunoy is a mixture of geothermal brine and oil. The experiment at Reykjanes, a volcanic geothermal area, exposed the samples to a separated vapour state 200 °C and 18 bar geothermal fluid, resulting in a visually homogeneous appearance after exposure. The Chaunoy experiment, performed in a sedimentary basin, on the other hand, exposed the materials to a 94 °C and 9.5 bar liquid state geothermal fluid.

The duration of the exposure was 1 and 4 months for Reykjanes and Chaunoy, respectively. The Reykjanes geothermal exposure conditions are substantially more severe, resulting in similar or more affected samples compared to Chaunoy.

The microstructure analysis of 316L at Reykjanes showed the formation of two inhomogeneous layers where the inner layer is Cr and Mo rich, and the outer layer contains Fe segregation. The 316L tested in Chaunoy showed local corrosion of around 4 μm in diameter and 2.5 μm in depth. The 254SMO tested in both locations showed subsurface elongated cracks of approximately 100 μm and longer.

The cracks in the 254SMO tested at Reykjanes showed a Cr rich layer forming within them as well as areas where material is breaking off. Corrosion was not observed on the surface of the Inconel 625 after Reykjanes testing. After both exposures, the material showed subsurface cracking. The Ti gr. 2 samples tested both in Reykjanes and Chaunoy showed an indication of erosion. The results are both supported by topography and cross-section images.

Even though all tested materials showed defects after exposures at both locations, no defect was observed to reach deeper than 50 μm into the coupon samples. Further testing is required to accurately predict the long-term sustainability of the tested materials for usage in heat exchanger plates at the tested locations and to investigate how the different defects evolve over time.

Author Contributions: Conceptualisation, S.D., B.G.G., K.B.K., B.A.L. and D.I.Ó.; Formal analysis, S.D.; Investigation, S.D.; Methodology, S.D. and D.I.Ó.; Project administration, D.I.Ó.; Supervision, D.I.Ó.; Writing—original draft, S.D.; Writing—geological context, K.B.K., B.G.G., D.I.Ó. and B.A.L.; Writing—review and editing, S.D., B.G.G., K.B.K., B.A.L. and D.I.Ó. All authors have read and agreed to the published version of the manuscript.

Funding: This research was funded by the European Union's Horizon 2020 research and innovation program and was part of the H2020 project MEET: Multidisciplinary and Multi-context Demonstration of EGS Exploration and Exploitation Techniques and Potentials. Call H2020-LCE-2017-RES-IA, grant number 792037.

Data Availability Statement: Not applicable.

Acknowledgments: We would like to thank Geir Þórólfsson in assisting with testing at Reykjanes as well as André-Charles Mintsa do Ango at Enogia and Eric Leoutre at Vermilion in assisting with testing at Chaunoy. We would also like to thank Helen Ósk Haraldsdóttir and Kolbrún Ragna Ragnarsdóttir for their contribution to the MEET project.

Conflicts of Interest: The authors declare no conflict of interest.

References

1. Sundén, B.; Manglik, R.M. *Plate Heat Exchangers: Design, Applications and Performance*, 11th ed.; Wit Press: Southampton, UK, 2007.

2. Nogara, J.; Zarrouk, S.J. Corrosion in geothermal environment: Part 1: Fluids and their impact. *Renew. Sustain. Energy Rev.* **2018**, *82*, 1333–1346. [CrossRef]
3. Wang, Z.; Paschalidou, E.M.; Seyeux, A.; Zanna, S.; Maurice, V.; Marcus, P. Mechanisms of Cr and Mo Enrichments in the Passive Oxide Film on 316L Austenitic Stainless Steel. *Front. Mater.* **2019**, *6*, 232. [CrossRef]
4. Cabrini, M.; Lorenzi, S.; Pastore, T.; Favilla, M.; Perini, R.; Tarquini, B. Materials selection for dew-point corrosion in geothermal fluids containing acid chloride. *Geothermics* **2017**, *69*, 139–144. [CrossRef]
5. Rafferty, K. Chapter 11: Heat Exchangers. In *Geothermal Direct Use: Engineering and Design Guidebook*; Oregon Institute of Technology: Klamath Falls, OR, USA, 1998; pp. 1–32.
6. Csaki, I.; Ragnasdottir, K.R.; Buzaianu, A.; Leosson, K.; Motoiu, V.; Guðlaugsson, S.; Lungu, M.V.; Haraldsdottir, H.O.; Karlsdottir, S.N. Nickel based coatings used for erosion-corrosion protection in a geothermal environment. *Surf. Coat. Technol.* **2018**, *350*, 531–541. [CrossRef]
7. Addepalli, S.; Eiroa, D.; Lieotrakool, S.; François, A.L.; Guisset, J.; Sanjaime, D.; Kazarian, M.; Duda, J.; Roy, R.; Phillips, P. Degradation Study of Heat Exchangers. *Procedia CIRP* **2015**, *38*, 137–142. [CrossRef]
8. Hattori, S.; Kitagawa, T. Analysis of cavitation erosion resistance of cast iron and nonferrous metals based on database and comparison with carbon steel data. *Wear* **2010**, *269*, 443–448. [CrossRef]
9. Mundhenk, N.; Scheiber, J.; Zorn, R.; Huttenloch, P.; Genter, A.; Kohl, T. Corrosion and Scaling in the Geothermal Cycle of Soultz-sous-Forêts (France). In Proceedings of the Corrosion 2014, San Antonio, TX, USA, 9–13 March 2014.
10. Ravier, G.; Seibel, O.; Pratiwi, A.S.; Mouchot, J.; Genter, A.; Ragnarsdottir, K.R.; Sengelen, X. Towards an optimized operation of the EGS Soultz-sous-Forêts power plant (Upper Rhine Graben, France). In Proceedings of the European Geothermal Congress 2019, Den Haag, The Netherlands, 11–14 June 2014.
11. Francesca Baticci, R.Z.; Genter, A.; Huttenloch, P. Corrosion and Scaling Detection in the Soultz EGS Power Plant, Upper Rhine Graben, France. In Proceedings of the World Geothermal Congress, Bali, Indonesia, 25–29 April 2010.
12. Sanjuan, B.; Millot, R.; Dezayes, C.; Brach, M. Main characteristics of the deep geothermal brine (5 km) at Soultz-sous-Forêts (France) determined using geochemical and tracer test data. *C. R. Geosci.* **2010**, *342*, 546–559. [CrossRef]
13. Ledésert, B.A.; Hébert, R.L.; Mouchot, J.; Bosia, C.; Ravier, G.; Seibel, O.; Dalmais, E.; Ledésert, M.; Trullenque, G.; Sengelen, X. Scaling in a Geothermal Heat Exchanger at Soultz-Sous-Forêts (Upper Rhine Graben, France): A XRD and SEM-EDS Characterization of Sulfide Precipitates. *Geosciences* **2021**, *11*, 271. [CrossRef]
14. Karlsdottir, S.N.; Ragnarsdottir, K.R.; Thorbjornsson, I.O.; Einarsson, A. Corrosion testing in superheated geothermal steam in Iceland. *Geothermics* **2015**, *53*, 281–290. [CrossRef]
15. Sarrade, S.; Féron, D.; Rouillard, F.; Perrin, S.; Robin, R.; Ruiz, J.C.; Turc, H.A. Overview on corrosion in supercritical fluids. *J. Supercrit. Fluids* **2017**, *120*, 335–344. [CrossRef]
16. Batis, G.; Kouloumbi, N.; Kotsakou, K. Corrosion and protection of carbon steel in low enthalpy geothermal fluids. The case of Sousaki in Greece. *Geothermics* **1997**, *26*, 65–82. [CrossRef]
17. Ungemach, P. Handling of corrosion and scaling shortcommings in low enthalpy geothermal environments. In Proceedings of the European Summer School on Geothermal Energy Applications, Oradea, Romania, 26 April–5 May 2001; pp. 113–127.
18. Stănăşel, I.; Stănăşel, O.; Gilău, L.; Sebeşan, M.; Gavriş, G. Control of Corrosion and Scaling in Selected Geothermal Wells from Romania. In Proceedings of the Proceedings World Geothermal Congress 2010, Bali, Indonesia, 25–29 April 2010.
19. ASTM G4-01. *Standard Guide for Conducting Corrosion Tests in Field Applications*; ASTM International: West Conshohocken, PA, USA, 2001; Volume 100.
20. Qurashi, M.S.; Cui, Y.; Wang, J.; Dong, N.; Bai, J.; Han, P. Erosion and passivation of borated 254 SMO stainless steel in simulated flue gas desulfurization solution. *Int. J. Electrochem. Sci.* **2020**, *15*, 2987–3002. [CrossRef]
21. Geary, E.A. *A Review of Performance Limits of Stainless Steels for the Offshore Industry*; Report 44; Health and Safety Laboratory: Derbyshire, UK, 2011.
22. Kritzer, P. Corrosion in high-temperature and supercritical water and aqueous solutions: A review. *J. Supercrit. Fluids* **2004**, *29*, 1–29. [CrossRef]
23. Neville, A.; Mcdougall, B.A.B. Erosion– and cavitation–corrosion of titanium and its alloys. *Wear* **2001**, *250*, 726–735. [CrossRef]
24. Khayatan, N.; Ghasemi, H.M.; Abedini, M. Study of Erosion–Corrosion and Corrosion Behavior of Commercially Pure-Ti During Slurry Erosion. *J. Tribol.* **2018**, *140*, 061609. [CrossRef]
25. Martelo, D.; Sampath, D.; Monici, A.; Morana, R.; Akid, R. Correlative analysis of digital imaging, acoustic emission, and fracture surface topography on hydrogen assisted cracking in Ni-alloy 625+. *Eng. Fract. Mech.* **2019**, *221*, 106678. [CrossRef]
26. Thorbjornsson, I.O.; Stefansson, A.; Kovalov, D.; Karlsdottir, S.N. Corrosion testing of materials in simulated superheated geothermal environment. *Corros. Sci.* **2020**, *168*, 108584. [CrossRef]
27. Karlsdottir, S. *Corrosion, Scaling and Material Selection in Geothermal Power Production*; Elsevier: Amsterdam, The Netherlands, 2012; pp. 241–259.
28. Nogara, J.; Zarrouk, S.J.; Seastres, J. Surface analysis of metal alloys exposed to geothermal fluids with high non-condensable gas content. *Geothermics* **2018**, *72*, 372–399. [CrossRef]
29. Nogara, J.; Zarrouk, S.J. Corrosion in geothermal environment Part 2: Metals and alloys. *Renew. Sustain. Energy Rev.* **2018**, *82*, 1347–1363. [CrossRef]

30. Sanada, N.; Lichtf, K.A. Prospects for the evaluation and development of materials under IEA research collaboration program on deep geothermal resources. In Proceedings of the NEDO International Geothermal Symposium, Sendai, Japan, 11–12 March 1997; pp. 192–199.
31. Wang, Q.; Wang, L.; Zhang, W.; Li, J.; Chou, K. Effect of Cerium on the Austenitic Nucleation and Growth of High-Mo Austenitic Stainless Steel. *Metall. Mater. Trans. B Process Metall. Mater. Process. Sci.* **2020**, *51*, 1773–1783. [CrossRef]
32. Van Der Eijk, C.; Walmsley, J.; Klevan, O.S.; Refinement, G.; Metals, R.E. Grain refinement of fully austenitic stainless STEELS using a Fe-Cr-Si-Ce master alloy. In Proceedings of the 59th Electric Furnace Conference, Phoenix, AZ, USA, 11–14 November 2001.
33. Al-Subai, S.G. Corrosion Resistance of Austenitic Stainless Steel in Acetic Acid Solution Containing Bromide Ions. Ph.D. Thesis, University of Manchester, Manchester, UK, 2011.
34. Giordani, E.J.; Guimarães, V.A.; Pinto, T.B.; Ferreira, I. Effect of precipitates on the corrosion-fatigue crack initiation of ISO 5832-9 stainless steel biomaterial. *Int. J. Fatigue* **2004**, *26*, 1129–1136. [CrossRef]
35. Wranglen, G. Pitting and sulphide inclusions in steel. *Corros. Sci.* **1974**, *14*, 331–349. [CrossRef]
36. Moorbath, S.; Sigurdson, H.; Goodwin, R. K-Ar ages of oldest exposed rocks in Iceland. *Earth Planet. Sci. Lett.* **1968**, *4*, 197–205. [CrossRef]
37. Vink, G.E. A hotspot model for Iceland an the Vøring Plateau. *J. Geophys. Res.* **1984**, *89*, 9949–9959. [CrossRef]
38. Thordarson, T.; Larsen, G. Volcanism in Iceland in historical time: Volcano types, eruption styles and eruptive history. *J. Geodyn.* **2007**, *43*, 118–152. [CrossRef]
39. Björnsson, S.; Arnórsson, S.; Tómasson, J. Exploration of the Reykjanes thermal brine area. *Geothermics* **1970**, *2*, 1640–1650. [CrossRef]
40. Sæmundsson, K.; Jóhannesson, H.; Hjartarson, Á.; Kristinsson, S.; Sigurgeirsson, M. *Geological map of SW-Iceland, 1:100 0000*; Iceland GeoSurvey: Reykjavík, Iceland, 2010.
41. Clifton, A.E.; Schlische, R.W. Fracture populations on the Reykjanes Peninsula, Iceland: Comparison with experimental clay models of oblique rifting. *J. Geophys. Res. Space Phys.* **2003**, *108*, 2074. [CrossRef]
42. Jakobsson, S.P. Chemistry and distribution pattern of recent basaltic rocks in Iceland. *Lithos* **1972**, *5*, 365–386. [CrossRef]
43. Pálmason, G.; Sæmundsson, K. Iceland in relation to the Mid-Atlantic Ridge. *Annu. Rev. Earth Planet. Sci.* **1974**, *2*, 25–50. [CrossRef]
44. Sæmundsson, K.; Sigurgeirsson, M.Á.; Friðleifsson, G.Ó. Geology and structure of the Reykjanes volcanic system, Iceland. *J. Volcanol. Geotherm. Res.* **2020**, *391*, 106501. [CrossRef]
45. Gudnason, E.A.; Agustsson, K.; Gunnarsson, K.; Flovenz, O.G. *Seismic Activity on Reykjanes December 2014–November 2015*; Report ÍSOR-2015/068; Iceland GeoSurvey: Reykjavík, Iceland, 2015; 31p.
46. Tómasson, J.; Kristmannsdóttir, H. High temperature alteration minerals and thermal brines, Reykjanes, Iceland. *Contrib. Miner. Petrol.* **1972**, *36*, 123–134. [CrossRef]
47. Franzon, H.; Thordardson, S.; Bjornsson, G.; Gudlaugsson, S.T.; Richter, B.; Fridleifsson, G.O.; Thorhallsson, S. Reykjanes High-temperature field SW-Iceland. Geology and hydrothermal alteration of well RN-10. In Proceedings of the 27th Workshop on Geothermal Reservoir Engineering, Stanford University, Stanford, CA, USA, 28–30 January 2002; pp. 233–240.
48. Berehannu, M.M. *Geochemical Interpretation of Discharge from Reykjanes Wells Rn-29 and Rn-32, Sw-Iceland*; United Nations University: Reykjavik, Iceland, 2014.
49. Brunet, M.-F.; Le Pichon, X. Subsidence of the Paris Basin. *J. Geophys. Res. Space Phys.* **1982**, *87*, 8547–8560. [CrossRef]
50. Courel, L.; Durand, M.; Maget, P.; Maiaux, C.; Menillet, F.; Pareyn, C. Trias. In *Synthèse Géologique Du Bassin Paris, Mémoire*; Mégnien, C., Ed.; BRGM: Orleans, France, 1980; Volume 101, pp. 37–74.
51. Eschard, R.; Lemouzy, P.; Bacchiana, C.; Desaubliaux, G.; Parpant, J.; Smart, B. Combining sequence stratigraphy, geostatistical simulations, and production data for modeling a fluvial reservoir in the Chaunoy field (Triassic, France). *Am. Assoc. Pet. Geol. Bull.* **1998**, *82*, 545–568.
52. Bourquin, S.; Friedenberg, R.; Guillochea, F. Depositional sequences in the Triassic series of the Paris Basin: Geodynamic implications. *J. Iber. Geol. Int. Publ. Earth Sci.* **1995**, *19*, 337–362.
53. Bourquin, S.; Guillocheau, F. Depositional sequences geometry of Keuper age (Ladinian to Rhaetian) of the Paris Basin—Geodynamic implications. *C. R. L Acad. Sci.* **1993**, *317*, 1341–1348.
54. Eschard, R.; Desaubliaux, G.; Lemouzy, P.; Bacchiana, C.; Parpant, J.; Chautru, J. Geostatistical simulations of alluvial sandbodies in the Triassic series of the Chaunoy field, France. In Proceedings of the American Association of Petroleum Geologists (AAPG) Mid-Continent Section Meeting, Amarillo, TX, USA, 10–12 October 1993. AAPG Bulletin.
55. Bacchiana, C.; Parpant, J.; Smart, B. Management of Chaunoy Oil Field Multilayered Reservoir. In *Hydrocarbon and Petroleum Geology of France*; Mascle, A., Ed.; Springer: Berlin/Heidelberg, Germany, 1994; pp. 147–153. [CrossRef]
56. Bourquin, S.; Rigollet, C.; Bourges, P. High-resolution sequence stratigraphy of an alluvial fan–fan delta environment: Stratigraphic and geodynamic implications—An example from the Keuper Chaunoy Sandstones, Paris Basin. *Sediment. Geol.* **1998**, *121*, 207–237. [CrossRef]
57. Karlsdottir, S.N.; Csaki, I.; Antoniac, I.V.; Manea, C.A.; Stefanoiu, R.; Magnus, F.; Miculescu, F. Corrosion behavior of AlCrFeNiMn high entropy alloy in a geothermal environment. *Geothermics* **2019**, *81*, 32–38. [CrossRef]

58. Mundhenk, N.; Knauss, K.; Bandaru, S.R.S.; Wonneberger, R.; Devine, T.M. Corrosion of carbon steel and the passivating properties of corrosion films formed under high-PT geothermal conditions. *Sci. Total Environ.* **2019**, *677*, 307–314. [CrossRef] [PubMed]
59. Ragnarsdóttir, K.R. Corrosion Experiments in Dry Superheated Steam From IDDP-1. Master's Thesis, University of Iceland, Reykjavik, Iceland, 2013.
60. Wang, Z.; Feng, Z.; Zhang, L. Effect of high temperature on the corrosion behavior and passive film composition of 316 L stainless steel in high H2S-containing environments. *Corros. Sci.* **2020**, *174*, 108844. [CrossRef]
61. Da Costa E Silva, A.L.V. The effects of non-metallic inclusions on properties relevant to the performance of steel in structural and mechanical applications. *J. Mater. Res. Technol.* **2019**, *8*, 2408–2422. [CrossRef]
62. Ganesan, P.; Renteria, C.M.; Crum, J.R. Versatile Corrosion Resistance of INCONEL Alloy 625 in Various Aqueous and Chemical Processing Environments. *Superalloys* **1991**, *718*, 663–680. [CrossRef]
63. Sundararaman, M.; Mukhopadhyay, P.; Banerjee, S. Carbide Precipitation in Nickel Base Superalloys 718 and 625 and Their Effect on Mechanical Properties. *Superalloys* **1997**, *718*, 625–706. [CrossRef]
64. Abd El Meguid, E.A.; Abd El Latif, A.A. Critical pitting temperature for Type 254 SMO stainless steel in chloride solutions. *Corros. Sci.* **2007**, *49*, 263–275. [CrossRef]
65. Ji, X.; Qing, Q.; Ji, C.; Cheng, J.; Zhang, Y. Slurry Erosion Wear Resistance and Impact-Induced Phase Transformation of Titanium Alloys. *Tribol. Lett.* **2018**, *66*, 64. [CrossRef]
66. Uz-Zaman, S. *Chemical Assessment of Icelandic Geothermal Fluids for Direct Applications*; United Nations Geothermal Training Programme; United Nations University: Reykjavik, Iceland, 2013.
67. Thomas, R. Titanium in the geothermal industry. *Geothermics* **2003**, *32*, 679–687. [CrossRef]
68. De, C. Use of Titanium and its Alloys in Sea-Water Service. *High Temp. Mater. Process.* **1993**, *11*, 61–96. [CrossRef]
69. Banker, J.G. *Titanium for Secondary Marine Structures*; International Titanium Association: Northglenn, CO, USA, 1996.